Icarus 221 (2012) 1089–1100

Contents lists available at SciVerse ScienceDirect

Icarus

journal homepage: www.elsevier.com/locate/icarus

Asteroid (2867) Steins: Shape, topography and global physical properties from OSIRIS observations

L. Jorda [a,*], P.L. Lamy [a], R.W. Gaskell [b], M. Kaasalainen [c], O. Groussin [a], S. Besse [a,1], G. Faury [a]

[a] Laboratoire d'Astrophysique de Marseille, UMR7326 CNRS/Aix-Marseille Université, 38 rue Frédéric Joliot-Curie, 13388 Marseille cedex 13, France
[b] Planetary Science Institute, 1700 East Fort Lowell, Suite 106, Tucson, AZ 85719, USA
[c] Department of Mathematics, Tampere University of Technology, PO Box 553, 33101 Tampere, Finland

ARTICLE INFO

Article history:
Available online 25 August 2012

Keywords:
Asteroids
Asteroids, Rotation
Asteroids, Surfaces

ABSTRACT

The Rosetta spacecraft flew by Asteroid (2867) Steins on 5 September 2008, allowing the onboard OSIRIS cameras to collect the first images of an E-type asteroid. We implemented several three-dimensional reconstruction techniques to retrieve its shape. Limb profiles, combined with stereo control points, were used to reconstruct an approximate shape model. This model was refined using a stereophotoclinometry technique to accurately retrieve the topography of the hemisphere observed by OSIRIS. The unseen part of the surface was constrained by the technique of light curves inversion.

The global shape resembles a top with dimensions along the principal axes of inertia of $6.83 \times 5.70 \times 4.42$ km. It is conspicuously more regular than other small asteroids like (233) Eros and (25143) Itokawa. Its mean radius is $R_m = 2.70$ km and its equivalent radius (radius of a sphere of equivalent volume) is $R_v = 2.63$ km. The north pole is oriented at RA = 99 ± 5° and Dec = −59 ± 5°, which implies a very large obliquity of 172° and a retrograde rotation.

Maps of the gravitational field and slopes were calculated for the well-imaged part of the asteroid. Together with the shape, they helped characterizing the most prominent topographic features identified at the surface of (2867) Steins: an equatorial ridge restricted to the extremities of the long axis, a large crater having dimensions of 2100×1800 m in the southern hemisphere, and an elongated hill in the northern hemisphere. We conjecture that the equatorial ridge was formed by centrifugal acceleration as the asteroid was spun up by the Yarkovsky–O'Keefe–Radzievskii–Paddack effect.

1. Introduction

Asteroids constitute a large population of objects whose progenitors were formed at the early stage of the birth of the Solar System. The present state of this population results from a long and complex history of dynamical, collisional and chemical evolution of these progenitors. The detailed study of individual asteroids is expected to give new insights into these processes.

Asteroid (2867) Steins (hereafter "Steins") has been selected as the first target of European Space Agency's Rosetta mission on its way to its final and main target, Comet 67P/Churyumov–Gerasimenko. An observing campaign of the asteroid has been organized prior to its flyby in order to characterize its properties and help prepare and optimize the Rosetta flyby. Visible and infra-red spectra and light curves have been obtained with several ground-based telescopes, and in the thermal infrared with the Spitzer Space Telescope (Lamy et al., 2008a,b). The analysis of these data yielded its main physical properties as summarized in Table 2: an approximatively spheroidal shape with major axis of 5.7, 5.0 and 4.6 km (i.e., a mean radius of 2.46 km), and a geometric albedo of 0.40 ± 0.07 in the R-band (Lamy et al., 2008b). The spectra are compatible with a surface composed of enstatite achondrites (Barucci et al., 2008), although they are slightly redder than previously observed E-type asteroids (Weissman et al., 2008). On the basis of all available observations, Steins has been classified as an E-type asteroid (Barucci et al., 2008), a rare class of objects never visited by a spacecraft. Enstatite can only form above 1000 °C, implying that Steins is a fragment of a larger differentiated body (Keller et al., 2010).

The aim of the Rosetta flyby was to better understand the formation and evolution of Steins through spatially resolved observations of its surface at wavelengths ranging from the far ultra-violet to millimeters. In this article, we present (i) the determination of the global shape model of Steins constructed from the images obtained with the OSIRIS visible cameras during the flyby combined with the inversion of all available light curves, (ii) the deduced bulk physical properties and (iii) a comprehensive survey of the main topographic features. Local slopes and gravitational heights are

* Corresponding author.
E-mail address: laurent.jorda@oamp.fr (L. Jorda).
[1] Present address: University of Maryland College Park, MD 20742, USA.

0019-1035/$ - see front matter © 2012 Elsevier Inc. All rights reserved.
http://dx.doi.org/10.1016/j.icarus.2012.07.035

calculated over the well imaged portion of the asteroid in order to refine the geological interpretation of the surface.

2. Observations

2.1. The OSIRIS imaging system

The "OSIRIS" Optical Spectroscopic and Infrared Remote Imaging System (Keller et al., 2007) is composed of two scientific cameras. The Narrow Angle Camera (thereafter "NAC") is a three-mirror anastigmat telescope with a field-of-view of 2.2°, a focal length of 717 mm and a focal ratio of 8. The Wide Angle Camera (thereafter "WAC") is a two-mirror off-axis telescope with a field-of-view of 12°, a focal length of 130 mm and a focal ratio of 5.6. Both telescopes have unobstructed apertures. The point-spread-function of the NAC and WAC cameras have FWHM of respectively 1.8–2.2 pixels and 1.5–1.7 pixels depending upon the filter bandpass. Both cameras are equipped with a dual filter wheel and an E2V 42–40 backlit, back-thinned CCD detectors of 2048×2048 pixels of 13.5 μm. The corresponding pixel field-of-view is 18.8 μrad for the NAC and 99.5 μrad for the WAC.

2.2. Pre-flyby observations

Pre-flyby observations of Steins started in early August 2008 for navigation purposes. The aim was to obtain high accuracy astrometric measurements of the asteroid from several NAC images a few weeks before closest approach, in order to refine its orbit and optimize the flyby distance at closest approach.

In addition, two uninterrupted light curves with high signal-to-noise ratio were also obtained before the flyby (Table 1). The aim was to extend the available data set with viewing geometries different from Earth so as to refine the part of the shape that would not be seen during the flyby by the technique of light curve inversion (see Section 3.1), and to accurately determine the rotational phase of the asteroid during the flyby. Two series of 144 images separated by 5 min and covering a time interval of 12 h, about twice the rotation period of the asteroid (Table 2), were thus acquired with both cameras 2 weeks and 24 h before closest approach, just before Steins could be resolved by the NAC. The journal of these observations is presented in Table 1. The first light curve was obtained with the F22 filter combining an orange filter centered at 625 nm with a bandpass of 85 nm, and a clear filter. For the second light curve, the clear filter was replaced by a neutral density filter to avoid saturating the detector. The processing of the images follows the procedure already implemented for similar observations of Steins performed in 2006 (Jorda et al., 2008) and of Asteroid (21) Lutetia in 2007 (Lamy et al., 2010); see also Section 2.4 below. The resulting light curves are displayed as time series of the reduced magnitude $R(1,1,\alpha)$ corresponding to the R photometric band of the Johnson–Kron-Cousins system in Fig. 1.

2.3. Flyby observations

The Rosetta spacecraft flew by Asteroid Steins on 5 September 2008 at a relative velocity of 8.6 km s^{-1}. The asteroid was actively tracked by the navigation cameras throughout the flyby in order to keep it in the field-of-view of the scientific instruments. The flyby campaign started at approximately 16:40 UT, Steins being at a distance of ~60,000 km from the spacecraft and at a phase angle of 37.8°. The first NAC images had a spatial scale of ~1 km per pixel.

Table 2
Pre-flyby main physical parameters of Asteroid (2867) Steins determined from ground- and space-based observations (Lamy et al., 2008a,b).

Parameter	Value
Mean radius	$R = 2.46 \pm 0.20$ km
Dimensions	$2a = 5.7 \pm 0.5$ km
	$2b = 5.0 \pm 0.5$ km
	$2c = 4.6 \pm 0.4$ km
Geometric albedo	$p_R = 0.40 \pm 0.07$
Sidereal period	$P_{sid} = 6.04681 \pm 0.00002$ h
Direction of spin axis	$\lambda = 250°$, $\beta = -89°$ (±5°) (ecliptic)
	RA = 91°, Dec = −67° (equatorial)

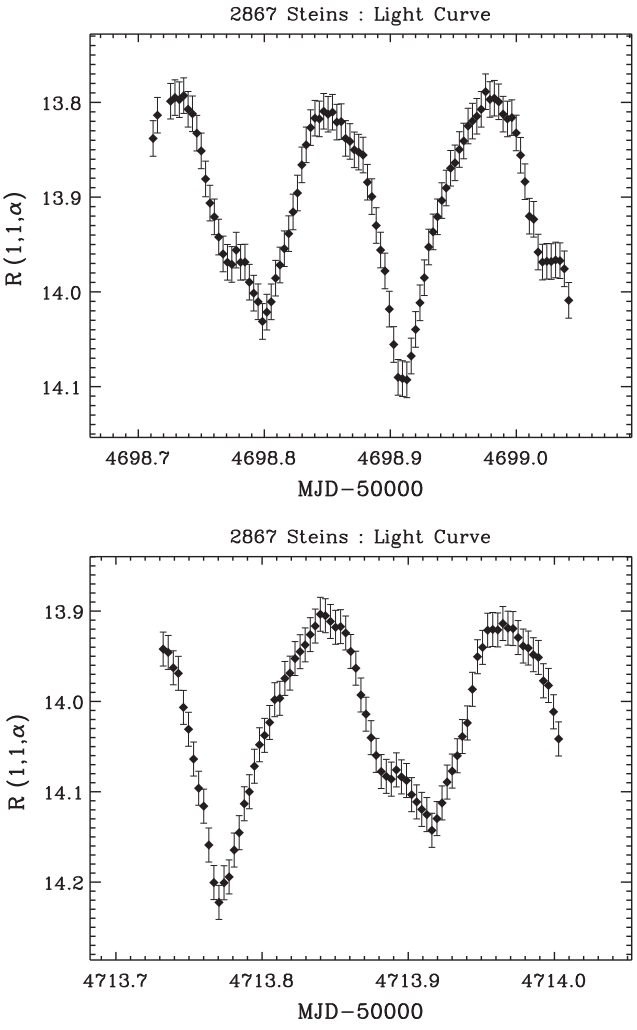

Fig. 1. Light curves of Asteroid (2867) Steins obtained on 20 August 2008 (top) and 4 September 2008 (bottom), respectively 2 weeks and 24 h before the Rosetta flyby. R-magnitudes reduced to 1 AU from the Sun and from Rosetta are plotted versus the modified Julian date.

Table 1
Geometric parameters of the pre-flyby images that yielded the two light curves used to reconstruct the global shape of Asteroid (2867) Steins.

Observations	Start obs. (UTC)	End obs. (UTC)	Range (km)	Phase angle (°)
LC #1	2008/08/20.711251	2008/08/21.041123	1.20×10^6–1.17×10^6	33.23–33.34
LC #2	2008/09/04.732298	2008/09/05.002858	77,500–57,400	38.13–38.20

Unfortunately, the NAC stopped its operations at 18:28:20 UT when the asteroid was still 5200 km away and the image scale had only reached ~100 m per pixel. The actual trajectory of the spacecraft with respect to the asteroid was reconstructed by the European Science Operation Center of ESA from OSIRIS images using additional star tracker measurements. The angle between the orbital plane and the equatorial plane of Steins was ~15°. The flyby was on the side of Steins rotating in the direction opposite to the spacecraft motion. The phase angle continuously decreased to reach a minimum value of 0.36° at 18:36:23 UT when the asteroid–spacecraft distance was ~1300 km. Closest approach occurred at 18:38:20 UT, at a distance of 803 km and a phase angle of 51°, the WAC images thus reaching the best spatial scale of 80 m per pixel. The OSIRIS flyby operations lasted ~4 h and stopped at about 20:30 UT, Steins being at a distance of 60,000 km and at a phase angle of 140°.

Throughout the flyby, the two cameras were operated in parallel (until the NAC stopped) at the maximum cadence of one image per 3 s and prominently with the orange filter (centered at 635 nm) combined with a neutral density for the NAC, and the "oxygen" filter (centered at 630 nm) for the WAC. In addition, sequences with additional filters were regularly inserted for color and mineralogic studies. Exposure times were set before the flyby in order to get a maximum of 10,000 DN per pixel. Altogether, 460 images were acquired by the OSIRIS cameras during the flyby.

2.4. Data reduction

All the images acquired by OSIRIS were reduced with the standard image reduction pipeline which, in its current version, performs the following operations:

- The electronic offset of the higher DN values ($\geqslant 2^{14}$ DN) produced by the "upper" analog-to-digital converter is subtracted.
- Coherent noise produced by the readout electronics is filtered out.
- The value of the offset corresponding to the binning and readout parameters of the image is subtracted.
- The image is divided by the flat-field of the filter configuration used during the image acquisition.
- The reduced DN values are then converted in units of spectral density of radiance using coefficients deduced from observations of standard stars (16 Cyg and Vega) during the commissioning of the instrument, and later on during several active checkouts and gravity assists.

This pipeline produces and stores radiometrically calibrated "level 2" images. A second pipeline is used to correct the images from the geometric distortion of the cameras. The directions of the line-of-sight of the undistorted pixels are projected in the CCD reference frame using optical distortion coefficients calculated from star fields acquired during the commissioning of the cameras. This gives a set of coordinates at which the pixel values of the distorted image are bi-linearly interpolated. This second pipeline therefore produces geometrically rectified "level 3" images. The error introduced during this process is usually lower than the photon noise error, except for high contrast regions near the limb or the terminator of the object.

3. Shape reconstruction

3.1. Models from light curve inversion

A shape model has been obtained prior to the flyby using the inversion technique of Kaasalainen et al. (2001) applied to a set of light curves obtained at various ground-based observatories, plus a light curve at a larger phase angle obtained with OSIRIS in March 2006 (Jorda et al., 2008). The method yielded an unscaled model which was then scaled in km using thermal fluxes measured with the Spitzer Space Telescope (Lamy et al., 2008a). This model was later refined by incorporating the two OSIRIS light curves obtained before closest approach (see Section 2.2 and Table 1).

3.2. Model from limb profiles

The limb can provide very useful constraints to reconstruct the shape of irregular objects, as for instance that of the nucleus of Comet 1P/Halley (Stooke and Abergel, 1991). The principle of this method is to use several limbs from different viewing angles in order to define the maximum convex hull of the body. This technique is often called "shape from silhouette" in specialized articles.

For Asteroid Steins, we applied this technique to one NAC and 59 WAC level 3 images, covering phase angles ranging from 30° to 0.4° on the inbound leg of the trajectory and then to 121° on the outbound leg. For each image, we defined the limb profile using an automatic procedure. We derived the contour of the body (limb and terminator) in two steps. First, a binary image with float values was created using a threshold which is a fraction of the maximum value of the signal. We then discriminated between limb and terminator testing the angle between the direction normal to the contour and that of the Sun projected in the image plane. The limb corresponds to the portion of the contour for which this angle is less than 90°. Once the limb profile of each image was defined, we proceeded to the three-dimensional shape reconstruction.

We started with a 4 km radius sphere defined by 32,400 triangular facets, a number large enough to fully inscribe the observed body. For a given image, we calculated the coordinates of the vertices of the triangular mesh in the camera frame. This required the absolute positions of the spacecraft and of Steins, the orientation of the camera and the rotational parameters of the asteroid in the J2000 equatorial reference frame. We then performed successive cylindrical cuts of the body, taking into account the constraint from the 60 limb profiles (Fig. 2) and were able to constrain about 60% of the surface. For the remaining non-illuminated part, we manually performed a smooth spherical extrapolation consistent with all images.

In order to account for the uncertainties in the reconstructed attitude of the spacecraft, we manually tuned the pointing of the camera to reach a good match between the observed images and the corresponding calculated ones. To do so, we took the spacecraft and asteroid positions reconstructed by ESA. Here again, we carefully checked afterwards that the resulting shape model was compatible with the whole set of images. Finally, the shape model was "regularized". The model in spherical coordinates was first resampled on a "hierarchical triangular mesh" (Kunszt et al., 2001) in Cartesian coordinates in order to remove the singularities at the poles. The surface of the facets were then homogenized by contracting the smallest edges into single points in an iterative process. We used an algorithm called "iterative contraction of edges", introduced during the last decades in computer graphics (e.g., Hoppe, 1996). Finally, the model was resampled in the reference frame defined by its principal axes of inertia assuming a constant density.

The shape model derived from limb constraints has a size of $6.7 \times 5.9 \times 4.3$ km, a surface of 93 km^2, and a volume of 76 km^3.

3.3. Model from control points

The Control Points (thereafter "CPs") technique to retrieve the shape of an object is well known since the early 1970s and has been applied to images of Mars (Davies, 1972) and Mercury (Da-

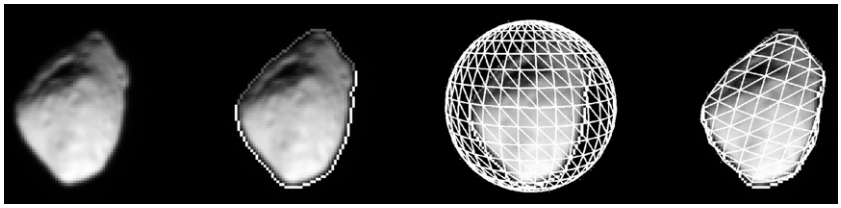

Fig. 2. Illustration of the "shape-from-silhouette" method. From left to right: (i) original image, (ii) determination of the limb profile, (iii) initial spherical shape model inscribing the asteroid, and (iv) final model resulting from a cylindrical cut along the profile.

vies and Batson, 1975). More recently, this technique has been extended to small, irregular bodies, for instance Gaspra (Thomas et al., 1994), Ida (Thomas et al., 1996), and to the nucleus of Comet 9P/Tempel 1 (Thomas et al., 2007). It is complementary to the limb method described above as it uses different information and as it allows defining the shape in additional areas. The constraint is given by the three-dimensional location of CPs distributed over the surface of the body. The CPs are nearly always associated with geological features such as craters and photometric anomalies.

For Steins, we used 13 images with pixel scales ranging from 80 to 112 m and phase angles from 27.5° to 95.3°. Images acquired later on are useless because they do not reveal any new part of the asteroid surface. To define the Cartesian coordinates of the CPs in the body-fixed frame, we proceeded in four steps (Besse, 2009):

1. We automatically detected points of interest using the "Fast Corner Detector" algorithm (Rosten et al., 2010,).
2. We matched the points of interest between two successive images by calculating the direction of the line-of-sight in the body-fixed frame at the time of the first image, from which we deduced by ray casting the coordinates of the point of interest in the body-fixed frame. This step required a preliminary shape model as input and we used the model defined by the limb constraints. We then predicted the image coordinates of this point in the second image and we defined a region of interest centered on it. Classic correlation techniques were then used to obtain tie points identified on at least two successive images.
3. We calculated the 3D coordinates of the control points in the body-fixed frame by intersecting the lines-of-sight of the tie points using the least-squares algorithm of Delvit et al. (2006). Note that the approximated body-fixed frame used at this step is modified later in Section 3.4.
4. We optimized the parameters defining the orientation of the camera using a least-squares Levenberg–Marquardt minimization algorithm, where the chi-square is the mean distance between the final CPs and the lines-of-sight of the tie points.
5. We went back to step 2 to perform a second iteration.

The above method allowed us to find the coordinates of 45 CPs distributed over the surface of Steins (Fig. 3) with a mean error of 20 m. The number of CPs was insufficient to define a global shape model, but they were used as an additional constraint to deform the limb model using the simplex mesh deformation method of Delingette (1997). This is possible, and in fact complementary as already underlined, since the two methods of reconstruction constrain different regions of the surface.

3.4. Model from stereophotoclinometry

The stereophotoclinometry (SPC) method developed by Gaskell et al. (2008a) has been applied to retrieve detailed topographic models of Asteroids (25143) Itokawa and (243) Eros (Gaskell, 2008), and can even accurately solve for the orbit and attitude of the spacecraft (Gaskell et al., 2008b). A detailed description can

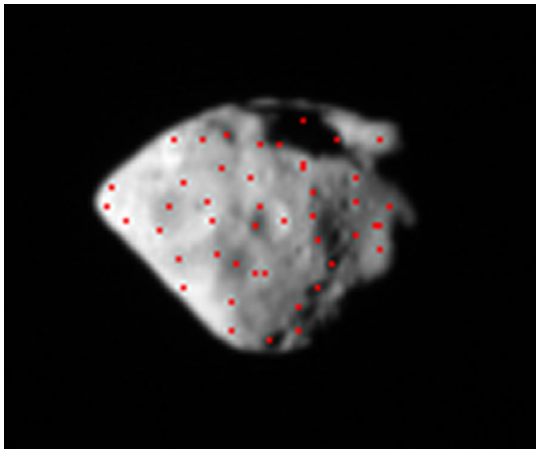

Fig. 3. Control points identified at the surface of Steins projected onto a WAC image obtained near closest approach.

be found in Gaskell (2006) and Gaskell et al. (2008b) in the frame of the Hayabusa mission. The SPC method was applied here to the set of 52 WAC images and the three NAC images obtained at the highest spatial resolution. The method works in several steps which are briefly summarized below.

The nominal geometric parameters – spacecraft and object positions and orientations – for each image were calculated from the SPICE kernels provided by ESOC. The rotational parameters were set to the pre-flyby values of Table 2. The surface of the previous model was then divided into several square "maplets", manually chosen from an image region or from a latitude–longitude grid. The size and resolution of the maplet were also chosen manually. Projected pixel values corresponding to the same maplet observed on several images were co-registered taking into account the viewing geometric parameters of each image. This allowed retrieving accurate stereographic coordinates of the maplet center and accurately determining the direction of the line-of-sight of the instrument for each image. Pixel values for the sub-part of the images corresponding to a given maplet were used to retrieve the slopes of the terrain around the center of the maplet, assuming a lunar law for the bi-directional reflectance (McEwen, 1996). The bi-directional reflectance function was assumed to be similar across the surface of the asteroid, except for the local single scattering albedo which was allowed to vary. A digital elevation map was then extracted from the slopes to create the digital terrain model corresponding to the maplet. Limb constraints were accounted for during the optimization process for each maplet. Note that the limb profiles used here were different from those used in Section 3.2. We proceeded by iteration until the maplets covered the whole visible surface and the convergence of all parameters was achieved. A global topographic model with a facet resolution of ~20 m was then created combining the elevation models of all the maplets. The pointing of the spacecraft and its position relative to the asteroid in the body-fixed frame were updated using the stereographic coordinates of the maplet centers, used here as CPs.

3.5. Global shape reconstruction

Because the length of the flyby was shorter than the rotational period of the asteroid, the imaging data covered only ~60% of the surface, leaving almost one hemisphere (~40%) undefined. In order to obtain a complete global shape model, this hemisphere was reconstructed using a variation of the multimodal data combination technique of Kaasalainen (2011). The vertices of the observed part of the surface were kept fixed, while the rotational parameters and the shape of the unobserved part were optimized to fit both the observed lightcurves and the limb and terminator contours of the OSIRIS images, imposing two additional regularization constraints: the smoothness of the shape model and a rotation around the principal axis corresponding to the largest moment of inertia (Kaasalainen, 2011). This ensured a consistent and smooth joining of the two shape parts. The reconstructed hemisphere has a resolution of only ~200 m. The transition between the two independently reconstructed hemispheres is not perfect so that the topography in this region presents artifacts.

For practical reasons, we homogenized the resolution of both hemispheres with a typical facet size of ~70 m, which matches that of the pixels of our highest resolution images. The final model is described by a mesh of 10,242 vertices and 20,480 triangular facets (Fig. 4).

3.6. Comparison of the different shape models

Fig. 6 displays observed and corresponding synthetic images generated from the different shape models. Three images acquired at different times are shown: the highest resolution NAC image (left panels), a WAC image obtained near CA (center panels) and one of the latest WAC images (right panels). The synthetic images have been generated with the "OASIS" simulator (Jorda et al., 2010) with the Hapke bi-directional reflectance parameters calculated by Spjuth et al. (2012) assuming a constant single-scattering albedo.

Our reconstruction offers an opportunity to test the light curve inversion technique by comparing our final SPC shape model with the pre-flyby model presented in Section 3.1. The comparison of the corresponding synthetic images of Fig. 5 shows that the pre-flyby model (second row) was not particularly successful in reproducing the global shape of the object. Its axis ratios amount to $a/b = 1.16$ and $a/c = 1.25$ to be compared with respectively 1.20 and 1.56 for the SPC model, i.e., a maximum discrepancy of ~20%. As emphasized by Lamy et al. (2008b), this is due to the restricted viewing geometries during the acquisition of the light curves. Steins was always seen close from equatorial aspect, yielding featureless light curves and resulting in a poorly constrained vertical dimension and a smooth shape model. The light curves alone simply do not contain much information (and this will be the case of any asteroids with similar spin direction and not coming close to the Earth) and we conclude that Steins does not offer a meaningful test for light curve inversion.

The limb model is intermediate between the pre-flyby model and the SPC model. It reproduces very well the global shape of Steins, in particular its "equatorial ridge". The dimensions (a and c) along the X- and Z-axes of the limb model are almost identical (within 1%) to those of our final SPC model. However, the dimension b along the Y-axis is 10% too large because the equatorial region around the Y-axis is not constrained by the limb profiles. As expected, neither the small topographic features observed at the surface of Steins nor the large crater Ruby are reproduced by the limb model.

Finally, synthetic images generated with our final SPC model are shown in the third row of Fig. 5 and they confirm that the model reproduces very well almost all the topographic features observed at the surface of Steins. It has however two limitations. First of all, the large crater Ruby is not deep enough in the SPC shape model as its floor is illuminated in the synthetic images whereas it is in shadow in the observed images. Second, small topographic details of a few pixels are not always reproduced in the final SPC shape model.

4. Global physical properties of Asteroid 2867 Steins

4.1. Global shape

The shape of Asteroid (2867) Steins resembles a top, with dimensions of $6.83 \times 5.70 \times 4.42$ km along the principal axes of inertia (see Section 4.2 below). The a/c axis ratio amounts to 1.56, a value significantly larger than that anticipated from the analysis of the light curves (see Section 3.6). The global shape is rather symmetric around the polar Z-axis, although there is a slight elongation of about 20% along the X-axis compared to the Y-axis. The a and b semi-major axis are ~15–20% larger than the predictions of Table 2, but there is a good agreement for the c axis. These differences are within the respective 1σ uncertainties of both measurements.

Steins has a size intermediate between the small Asteroid (9969) Braille observed by the Deep Space 1 spacecraft (Oberst et al., 2001) and the larger Asteroid (951) Gaspra observed by Galileo (Thomas et al., 1994). Its size is comparable to (5535) Annefrank observed by Stardust (Duxbury et al., 2004). The global shape presented in Fig. 4 is more regular than those of other asteroids, like (233) Eros (Thomas et al., 2002) and (25143) Itokawa (Demura et al., 2006). It is also less elongated than the aforementioned asteroids, which all have a/c axes ratios $\geqslant 1.9$.

4.2. Physical parameters

Once we have determined the shape model of the asteroid, it is possible to calculate its physical properties by means of surface and volume integrals. Surface integrals are calculated by summing the areas of the individual triangles which define the surface of the model. Volume integrals are calculated by summing the volume of the individual tetrahedra formed by these triangles and the center of figure of the object. The following quantities were calculated: the total surface and volume of Steins, the Cartesian coordinates of its center of mass and the components of its tensor of inertia. The latter was diagonalized in order to determine the moments of inertia (the eigenvalues) and the rotation matrix (the eigenvectors). The shape model was translated and rotated in the new coordinate system defined by the center of mass and by the three principal axes of inertia (thereafter PAIs). Assuming that Steins has a uniform density and is in a pure rotational state, its spin axis is then parallel to the principal axis corresponding to the largest moment of inertia, whose direction differs from that given in Table 2 (pre-flyby model) by only 5°. Note that, since the rotation is not clearly detectable on our images, this value remains affected by an uncertainty of several degrees. This uncertainty comes from errors in the individual data points of the photometric light curves used to retrieve the direction of the north pole and from the internal error associated to the technique of light curve inversion. The physical parameters are presented in Table 3. The intrinsic numerical error due to the discrete sampling of the surface is estimated at less than 1%, which is negligible compared to the error coming from the incomplete surface coverage. Assuming an uncertainty of 10% on the radii of the vertices of the unseen hemisphere yields an uncertainty of respectively ~10% and ~15% for the surface and volume integrals.

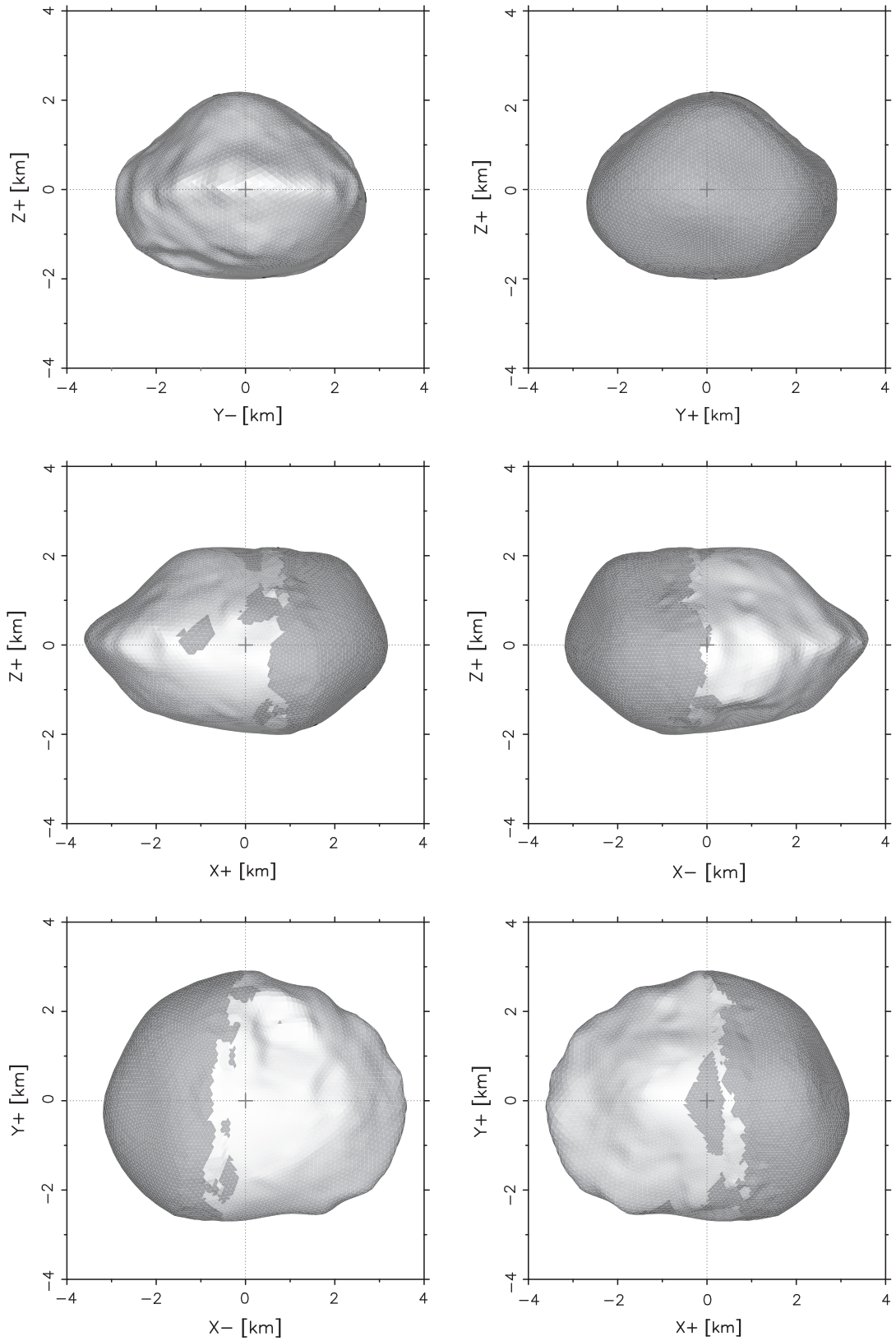

Fig. 4. Six views of the final shape model of (2867) Steins. The model has been shaded assuming a Lambertian scattering law for a better visualization of the topography. The light-grey region was reconstructed using the stereophotoclinometry technique, whereas the dark-grey region was constrained by light curves inversion. The squares in which the models are inscribed have sides of 8 km.

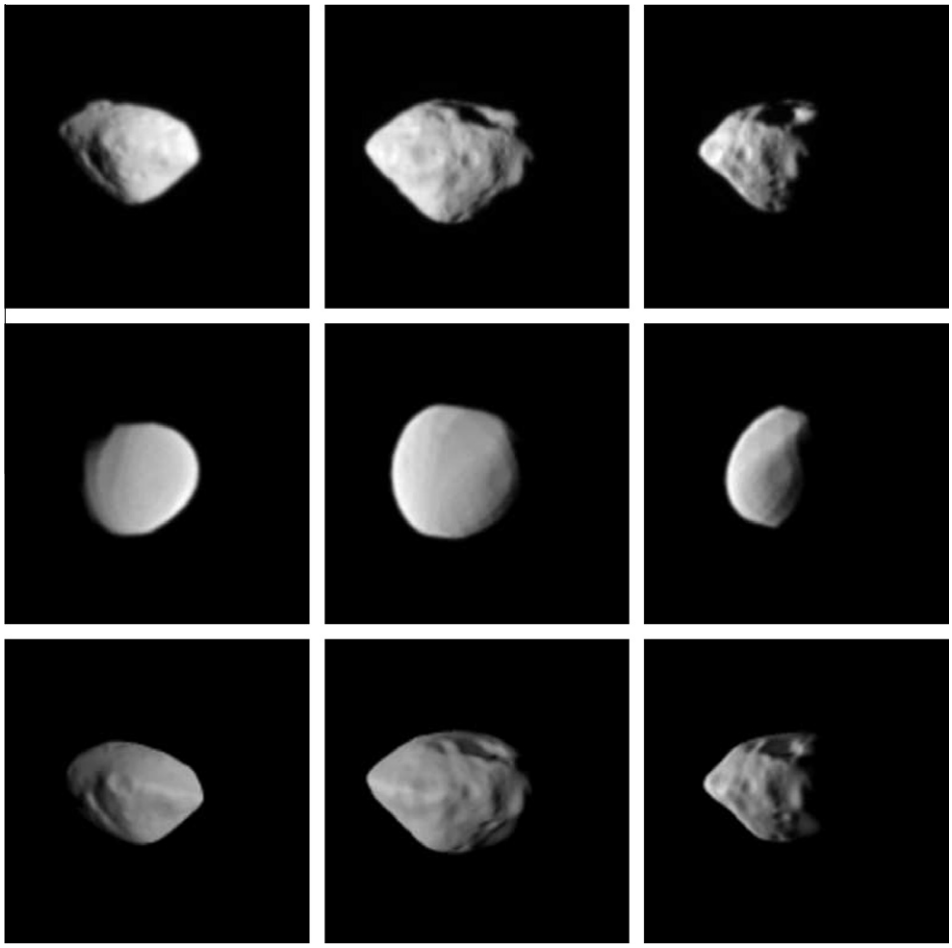

Fig. 5. Comparison of observed and synthetic images calculated from different shape models. First row: the highest resolution NAC image of Steins acquired at 18:28:19 UTC (left column), and two WAC images acquired at 18:37:56 UTC and 18:39:10 UTC. The three images correspond to respectively #5, #23 and #36 listed in Table 3 of the supplemental material associated to this article. Their overall fields-of-view are respectively 25.2 km, 20.3 km and 22.4 km. Second row: the corresponding simulated images created with our pre-flyby model determined by light curves inversion. Third row: simulated images created with the stereophotoclinometry model (see Section 3.4).

Table 3
Nominal values of the bulk physical and rotational parameters of Asteroid (2867) Steins calculated from its shape model assuming a constant density of 1800 kg m^{-3}.

Parameter	Value
Diameter along the PAIs	$2a \times 2b \times 2c = 6.8 \times 5.7 \times 4.4$ (±0.1) km
Best-fit ellipsoid	$2a \times 2b \times 2c = 6.5 \times 5.5 \times 4.1$ km
Mean radius	$R_m = 2.70$ km
Surface	$S = 92 \pm 9$ km^2
Volume	$V = 76 \pm 11$ km^3
Volume-equivalent radius	$R_v = 2.63 \pm 0.13$ km
Normalized moments of inertia	$I_1/M = 2.36$ km^2
	$I_2/M = 3.00$ km^2
	$I_3/M = 3.68$ km^2
Direction of spin axis	$\lambda = 94°$, $\beta = -85°$ (±5°) (ecliptic)
	RA = 91°, Dec = −62° (equatorial)
Direction of ($\lambda = 0$) axis	W = 321.76° + 1428.099174d[a]
Surface gravity	0.08 − 0.13 cm s^{-2}
Centrifugal acceleration	<0.03 cm s^{-2}
Maximum slope	35.0°

[a] Julian days since J2000.

5. Surface topography

5.1. General topographic properties

The general topography of Steins was first characterized by calculating the local value of several parameters derived from the shape model. We used our own implementation of the algorithm of Werner and Scheeres (1996) to determine the local gravitational and acceleration fields from the oversampled triangular mesh corresponding to the final SPC model of Section 3.5. We also calculated the local slopes, defined as the angles between the local normal to the surface and the local acceleration vector, sum of the gravitational acceleration and the centrifugal acceleration using the rotational parameters of Table 2. The slopes were calculated for each surface element of our final shape model, i.e., for a scale length of about 70 m. These calculations require the density of Steins which remains unknown. On the basis of its composition and likely rubble-pile structure (Keller et al., 2010), we adopted a density of 1800 kg m^{-3} obtained by combining the bulk density of enstatite achondrite meteorites $\rho \approx 3000$ kg m^{-3} (Macke et al., 2009) and a macro-porosity of ≈40% (Britt et al., 2002). The slopes are generally less than 15° across the surface, except along the equatorial ridge and inside the crater Ruby where the largest slope angles of ∼30° are observed. A histogram of the distribution of slopes is shown in Fig. 7. It was calculated using only the facets of the hemisphere seen during the flyby and taking into account the area of the individual facets. The distribution is comparable to that of Deimos and shows no clear enhancement at large slope angles, as observed at the surfaces of Asteroids (243) Ida (Thomas et al., 1996) and (25143) Itokawa (Fujiwara et al., 2006). The large extent of a smooth terrain with shallow slopes is consistent with the observed lack of photometric variations of the single scattering

albedo (Spjuth et al., 2012) and may result from the action of one or several mechanisms such as seismic shaking (Richardson et al., 2005) and the Yarkovsky–O'Keefe–Radzievskii–Paddack (thereafter YORP) effect to be also invoked later on to explain the equatorial ridge. These effects tend to spread out the regolith particles, which could have in turn "smoothed out" pre-existing photometric variations and steep slopes. Spatial segregation may still be present, but at scales smaller than our best image resolution (<200 m).

Fig. 6 displays a cylindrical representation of the surface constructed from two images projected using the final SPC shape model. The origin of the longitude is defined by the center of the crater Spinel located near the equator, following the convention adopted by Besse et al. (2012). At the edge of the body observed during the flyby (positive *X*-axis), near the equator, a prominent "equatorial ridge" can be seen extending over ~90° in longitude (label "a" in Fig. 6). The large "Ruby" crater (Besse et al., 2012) is clearly identified near the south pole on several WAC images and is labeled "b". A linear feature labeled "c" in Fig. 6 is observed in the northern hemisphere on the NAC images. A catena – chain of 7 aligned small "craters" of diameter 250–600 m – is well visible at west (negative) longitudes of 20–25°. We will not discuss in detail here the size distribution and the morphology of the craters observed at the surface of Steins as this is addressed in a separate article (Besse et al., 2012).

The low spatial resolution of the images and the small number of pixels across the asteroid hamper a detailed quantitative geologic study of the surface of Steins. In the following sections, we address the above main topographic, large-scale features based on our final shape model.

5.2. Equatorial ridge

The most prominent surface feature is a ridge forming a circular arc centered at longitude $\lambda = 55°$ and latitude $\phi = +1°$, i.e., almost equatorial. It conspicuously extends between longitudes 5° and 95° and progressively vanishes outside this range, i.e., near the terminator in the OSIRIS images. However, the half-hemisphere not seen by OSIRIS and therefore only constrained by the light curves does display a bulge at the same latitude (see the side view of Fig. 5). It is therefore likely that both features are connected and altogether result from the evolution of Steins.

Fig. 8 shows the local slopes, as defined in Section 4.2. The slopes within the ridge (in a band of ±500 m) exceed 15° to even reach 30°, in striking contrast with the rest of the surface, where the slopes are less than 15°.

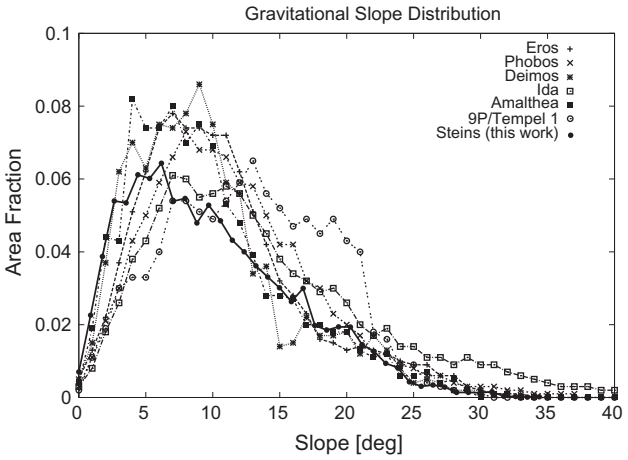

Fig. 7. Histogram of the slopes of Asteroid (2867) Steins and of small objects whose shape and topography have been determined from imaging instruments aboard space probes (Courtesy: P. Thomas). The slopes have been calculated for a scale length equal to the size of the facets, i.e., about 70 m assuming a uniform density of 1800 kg m^{-3}.

The most likely mechanism to form the ridge and explain the rather symmetric shape of Steins is the YORP effect (Harris et al., 2009), as already pointed out by Keller et al. (2010). This effect is capable of spinning up an object and in turn triggering material motion which can ultimately produce an axi-symmetric shape with a constant latitudinal slope of ~30–40° corresponding to the "critical slope" beyond which "landsliding" of material towards the equator occurs. The resulting shape exhibits a ridge at the equator, whereas the original shape of the body is relatively well preserved in the polar regions (Harris et al., 2009). Asteroids (66391) 1999 KW4 (Ostro et al., 2006) and 2008 EV5 (Busch et al., 2011) whose shapes were derived from radar imaging both exhibit an equatorial ridge which is also thought to result from YORP-induced spin up. These two near-Earth asteroids are much smaller than Steins, having equatorial diameters of respectively 1.5 km and 0.4 km.

We propose the following scenario for the formation of the ridge. The original shape of Steins was a slightly elongated prolate

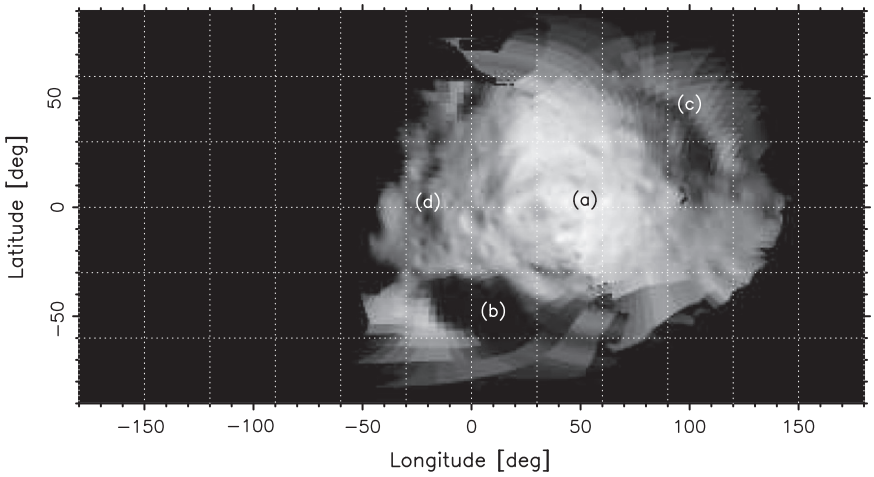

Fig. 6. Cylindrical projection of the surface of Asteroid (2867) Steins observed during the flyby. This map was built by projecting the pixel values of the highest resolution NAC image and those of a WAC image acquired at closest approach onto the surface elements of the shape model of Fig. 4, plotted here in spherical coordinates. The most prominent topographic features are: the equatorial ridge (a), the large crater Ruby (b), the northern hill (c), and the catena of craters (d). The surface in black has not been observed during the flyby. Longitudes increase towards the East.

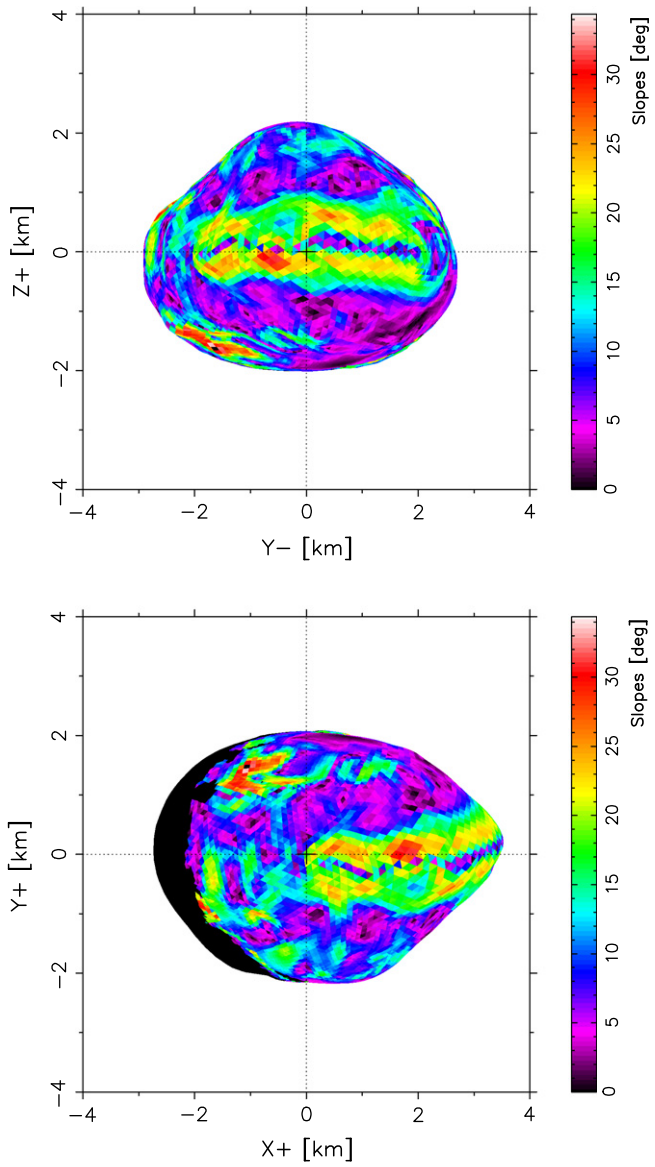

Fig. 8. Two maps of the slope angle at the surface of Asteroid (2867) Steins. The top map corresponds to the top left view displayed in Fig. 4. The bottom map corresponds to the image displayed at the center of the first row in Fig. 5. For the latter map, the *X* and *Y* axes refer to projected image coordinates. The slopes have been calculated for a scale length equal to the size of the facets, i.e., about 70 m assuming a uniform density of 1800 kg m^{-3}.

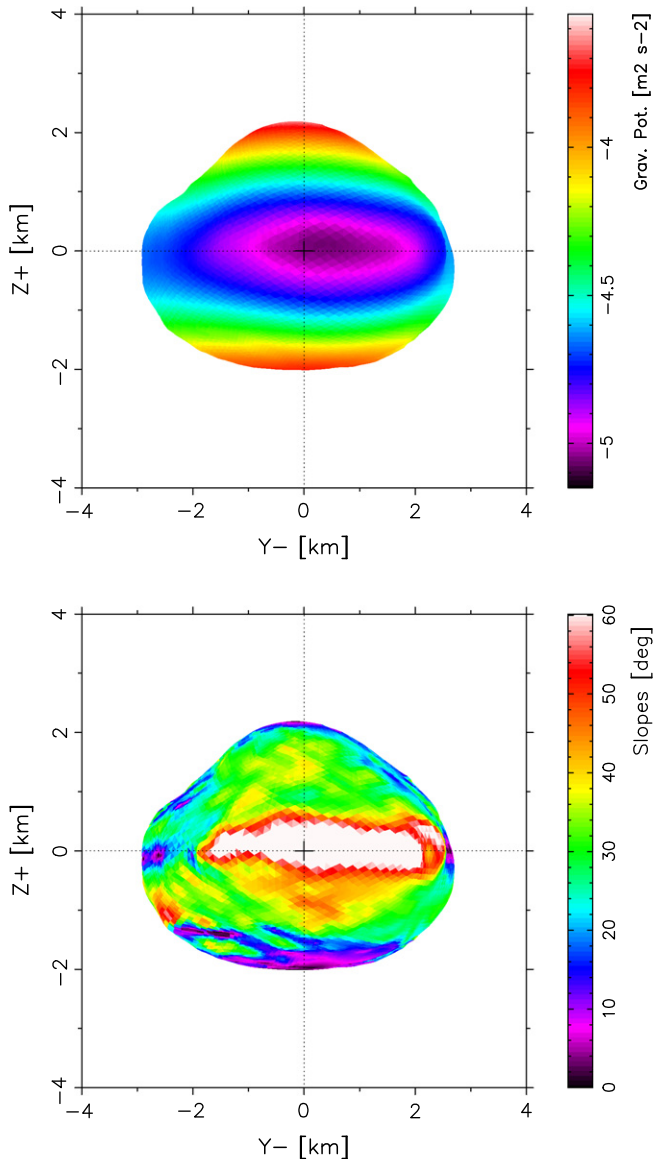

Fig. 9. Maps of the gravitational potential (top) and of the slopes (bottom) at the surface of Asteroid (2867) Steins calculated from the SPC shape model assuming an hypothetical rotational period of 3 hr produced by the YORP effect.

body. The YORP effect first decreased its spin period to a value well below 4 h, for which the centrifugal acceleration started to induce an equatorial bulging along its largest axis. This is illustrated in Fig. 9, where we show the gravitational potential and slopes for a spin period of 3 h. In striking contrast to the present situation, the gravitational potential is dominated by the centrifugal acceleration which results in an area of low potential located exactly at the equatorial ridge where the regolith can therefore accumulate. The slopes in the southern and northern flat terrains at intermediate latitudes on both sides of the ridge amount to 30–45°, a range sufficient to trigger downslope motion towards the ridge. The slopes in the polar regions remain less than 15°, implying that the original shape has been preserved in these regions. However and perhaps due to its size, the spin period did not decrease to the point of entirely reconfiguring the original Steins, which would have likely resulted in a complete circular ridge. At the same time, the YORP effect progressively moved the direction of the spin axis, modifying its obliquity. As the shape and the obliquity changed, the torque associated to the YORP effect eventually became negative, thus causing a spin-down of the asteroid on a timescale of $\sim 10^7$–10^8 years (Rubincam, 2000). The spin period of Steins measured nowadays is the result of this slow spin-down.

A dedicated modeling of the YORP effect and of its influence on the shape of Steins is required to test this scenario but is beyond the scope of the present study.

5.3. Crater Ruby

The largest crater called "Ruby" (Fig. 6) is observed in the south pole region, at latitude $\phi = +50°$ and longitude $\lambda = 10°$. The topography of this region is difficult to retrieve because it has been observed only at grazing angles during the flyby, and the floor of the crater remained in shadow. The rim itself is well pronounced and appears quite irregular both on images, as already pointed out by Besse et al. (2012), and on the shape model. This may result

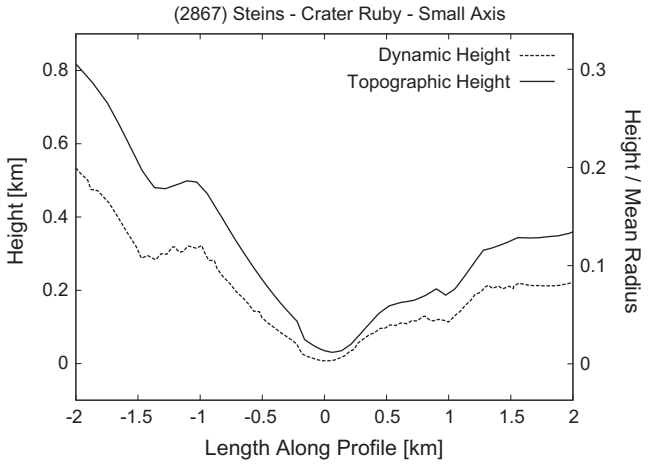

Fig. 10. Topographic (solid line) and dynamic (dashed line) height profiles through the crater Ruby along the line-of-sight at closest approach. The heights are displayed in physical units (km, left scale) and in units of Steins' mean radius (right scale). These profiles have been extracted parallel to the "*X*-"axis of the bottom left panel of Fig. 4, which corresponds to the smallest dimension of the crater.

from smaller craters pitting the rim as recorded on other large craters such as Karoo on (253) Mathilde and Stickney on Phobos. Ruby seems to be slightly elongated along the *X*-axis of the body-fixed frame. From the shape model, we estimated the dimensions of the inner rim to be 1700×1400 m with an uncertainty of ±100 m, and the width of the rim to be 200 ± 30 m. Therefore, the total dimensions of the crater are $\sim 2100 \times 1800$ m (±100 m). Using the relative size $F = D/R_m$ introduced by Thomas et al. (1999), where D is the crater mean diameter and R_m is the object mean radius, we found $F = 0.77$ which is much less than the largest craters observed on Deimos ($F = 1.6$) and on (253) Mathilde ($F = 1.26$); in fact, Ruby is closer to the largest craters observed on (243) Ida ($F = 0.88$) and Phobos ($F = 0.85$).

Fig. 10 presents a profile across Ruby essentially along the line-of-sight at CA (the section perpendicular to the line-of-sight is poorly defined and therefore omitted). We display the topographic and dynamic heights, the latter corresponding to gravitational topography which is proportional to potential energy at the surface due to the sum of self-gravity and centrifugal acceleration. As emphasized by Thomas et al. (1999), gravitational topography is essential for studying irregularly shaped objects as topographic profiles give very misleading indications of slopes relative to the local surface acceleration. The profile suggests a classical bowl-shaped morphology with however a marked asymmetry. We estimated a maximum (topographic) depth of ~290 m, but this is a lower limit since the floor of the crater has not been imaged; dynamically, it is only ~190 m, here again a lower limit. From a photometric comparison of simulated and observed images, Besse et al. (2012) have estimated a (topographic) depth of ~300 m assuming a perfect bowl shape, which is indeed compatible with our limit of ~290 m.

The asymmetric profile is somewhat reminiscent of that of the large crater on Deimos possibly indicating some (partial) infill (Thomas et al., 1999), although no photometric variations have been detected inside the crater (Spjuth et al., 2012). The largest slopes at the surface of Steins are located in the inner rim of Ruby and range from 25° to 36° in an area of about 0.2 km^2. A significant fraction of the surface at this location has therefore slopes larger than the typical values of ~30° expected for the angle of repose of regolith particles (Richardson et al., 2005).

5.4. Northern hill

A bright, elongated feature is conspicuously seen on the NAC images obtained before CA (see upper left image of Fig. 5) as well as on the corresponding synthetic images (see bottom left image of Fig. 5). The corresponding structure on the shape model is located in the northern hemisphere of the asteroid, with its center at longitude $\lambda = 100°$ and latitude $\phi = +45°$ (Fig. 6), that is 125° away from the center of the large crater Ruby, and appears as an elevation of 120–150 m extending quasi-linearly over ~2 km (Fig. 11). This region is only constrained by the photoclinometric information extracted from a small subset of NAC images acquired at a unique geometry (i.e., no stereographic information), so that its interpretation requires some caution. It is a priori possible that this feature corresponds to the partial rim of a crater which would have a diameter of at least 2 km, that is the size of Ruby. There are however two arguments against this interpretation. First, such a crater would imply a very large excavation extending to the left side of this feature in Fig. 11, whereas both the images and the model only suggest a rather narrow depression. Second, it would have a semi-circular shape and we would therefore expect the incident angle between the local normal to the surface and the direction of the solar radiation to vary. This would imply a variation of its radiance which is not detected within ±15%. We are therefore inclined to interpret this feature as an isolated, elongated "hill". According to the scenario proposed by Keller et al. (2010), Steins

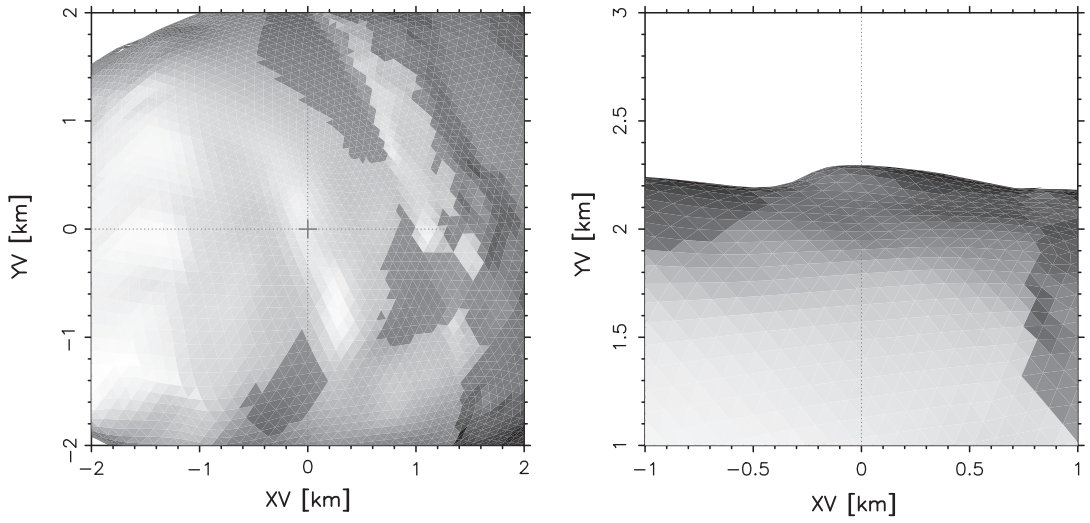

Fig. 11. Zoom on the SPC shape model in the region of the northern hill (left) and side view of the same region (right) which highlights its profile.

was already strongly fractured or even a rubble pile when the large impact that created crater Ruby occured and definitively transformed it in the latter state; this is required to allow for the YORP effect to subsequently produce the present "top" shape. It is therefore conceivable that the above feature corresponds to a very large monolithic fragment that emerged from the surrounding pile of smaller pieces either by direct pressure exerted by the impactor of the crater Ruby (the hill is approximately diametrically opposite to that crater) or the spreading of the surrounding smaller fragments as the reshaping proceeded. Limited illumination conditions precluded the photometric characterization of this region (Spjuth et al., 2012), so that we cannot decide whether we actually see a bare fragment protubing above the surrounding regolith layer, or whether it is somewhat below the surface and covered by the general regolith layer. The relatively gentle slopes of the hill ($\leqslant 25^\circ$) indeed allows the second alternative.

6. Conclusion

Asteroid (2867) Steins was imaged at limited spatial resolution by the OSIRIS cameras during the September 2009 flyby by the Rosetta spacecraft. We used several three-dimensional reconstruction techniques to retrieve its shape and topography. Limb profiles, combined with stereo control points, were first used to reconstruct an approximate shape model. This model was refined using a stereophotoclinometry (SPC) technique to retrieve the exact topography of the hemisphere observed by OSIRIS (precisely 60% of the surface) with a facet resolution of $\sim$20 m. The unseen part of the surface was modeled by light curves inversion imposing a smooth connection with the SPC model and has a resolution of $\sim$200 m. Altogether, they produced a complete shape model of Steins, demonstrating the power of combining these complementary techniques.

Our main results are summarized below:

- The global shape of Asteroid (2867) Steins is approximately axially symmetric around its polar axis and resembles a top.
- The main topographic features are an equatorial ridge, the large crater Ruby located near the south pole, a linear feature in the northern hemisphere interpreted as a hill and a catena of 7 aligned small craters roughly oriented in the north–south direction.
- The large extent of the smooth terrain with shallow slopes ($<15^\circ$) is consistent with the observed lack of photometric variations of the single scattering albedo (Spjuth et al., 2012) and may result from the action of one or several mechanisms such as seismic shaking and spin up induced by the Yarkovsky–O'Keefe–Radzievskii–Paddack (YORP) effect. This effect could also explain the formation of the equatorial ridge.
- The "northern hill" is only constrained by photoclinometry but its interpretation as a partial rim of a crater is excluded. It may be explained by a very large fragment of the rubble pile either displaced near or to the surface by the Ruby impactor or which later appeared under the action of YORP reshaping.

Altogether, our results are consistent with the conclusion of Keller et al. (2010) that Asteroid (2867) Steins must be a rubble pile. This will be further elaborated in a forthcoming article.

Acknowledgments

S. Besse was supported by a doctoral fellowship jointly funded by CNES (Centre National d'Etudes Spatiales) and Thales Alenia Space. We are grateful to S. Spjuth for providing the cylindrical projection of (2867) Steins. OSIRIS was built by a consortium of the Max-Planck-Institut für Sonnensystemforschung, Lindau, Germany, the Laboratoire d'Astrophysique de Marseille, France, the Centro Interdipartimentale Studi e Attivita' Spaziali, University of Padova, Italy, the Instituto de Astrofisica de Andalucia, Granada, Spain, the Research and Scientific Support Department of the European Space Agency (ESA/ESTEC), Noordwijk, The Netherlands, the Instituto Nacional de Tecnica Aerospacial, Madrid, Spain, the Institut für Datentechnik und Kommunikationsnetze der Technischen Universität, Braunschweig and the Department of Astronomy and Space Physics of Uppsala University, Sweden. The support of the national funding agencies DLR, CNES, ASI, MEC, NASA, and SNSB is gratefully acknowledged. We thank the Rosetta Science Operations Center and the Rosetta Mission Operations Center for the successful flyby of (2867) Steins. We thank J. Oberst and an anonymous referee for fruitful comments which significantly improved this article.

References

Barucci, M.A. et al., 2008. Asteroids 2867 Steins and 21 Lutetia: Surface composition from far infrared observations with the Spitzer Space Telescope. Astron. Astrophys. 477, 665–670.
Besse, S., 2009. Reconstruction tri-dimensionnelle des petits corps du système solaire. PhD Dissertation.
Besse, S., Lamy, P., Jorda, L., Barbieri, C., 2012. Identification and physical properties of craters on Asteroid (2867) Steins. Icarus, submitted for publication.
Britt, D.T., Yeomans, D., Housen, K., Consolmagno, G., 2002. Asteroid density, porosity, and structure. In: Bottke, W.F., Paolicchi, P., Binzel, R.P., Cellino, A. (Eds.), Asteroids III. Univ. of Arizona Press, Tucson, AZ, pp. 485–500.
Busch, M.W. et al., 2011. Radar observations and the shape of near-Earth Asteroid 2008 EV5. Icarus 212, 649–660.
Davies, M.E., 1972. Coordinates of features on the mariner 6 and 7 pictures of Mars. Icarus 17, 116–167.
Davies, M.E., Batson, R.M., 1975. Surface coordinates and cartography of Mercury. J. Geophys. Res. 80, 2417–2430.
Delingette, H., 1997. General Object Reconstruction based on Simplex Meshes. INRIA Technical Report No. 3111.
Delvit, J.-M., Fave, P., Gachet, R., 2006. The geometric supersite of Salon de Provence. In: Symposium of ISPRS Commission I, vol. 181, pp. 19–24.
Demura, H. et al., 2006. Pole and global shape of 25143 Itokawa. Science 312, 1347–1349.
Duxbury, T.C. et al., 2004. Asteroid 5535 Annefrank size, shape, and orientation: Stardust first results. J. Geophys. Res. (Planets) 109, E02002.
Fujiwara, A. et al., 2006. The rubble-pile Asteroid Itokawa as observed by Hayabusa. Science 312, 1330–1334.
Gaskell, R.W. et al., 2006. Landmark navigation studies and target characterization in the Hayabusa encounter with Itokawa. AIAA/AAS Astrodynamics Specialist Conference and Exhibit. Abstract #6660.
Gaskell, R.W., 2008. Gaskell Eros Shape Model V1.0. NASA Planetary Data System 96.
Gaskell, R. et al., 2008a. Gaskell Itokawa Shape Model V1.0. NASA Planetary Data System 92.
Gaskell, R.W. et al., 2008b. Characterizing and navigating small bodies with imaging data. Meteorit. Planet. Sci. 43, 1049–1061.
Harris, A.W., Fahnestock, E.G., Pravec, P., 2009. On the shapes and spins of "rubble pile" asteroids. Icarus 199, 310–318.
Hoppe, H., 1996. Progressive meshes. In: Proc. SIGGRAPH'96, pp. 99–108.
Jorda, L. et al., 2008. Asteroid 2867 Steins. I. Photometric properties from OSIRIS/Rosetta and ground-based visible observations. Astron. Astrophys. 487, 1171–1178.
Jorda, L., Spjuth, S., Keller, H.U., Lamy, P.L., Llebaria, A., 2010. OASIS: A simulator to prepare and interpret remote imaging of Solar System bodies. In: Proc. SPIE, vol. 7533, no. 753311.
Kaasalainen, M., 2011. Multimodal inverse problems: Maximum compatibility estimate and shape reconstruction. Inverse Probl. Imag. 5, 37–57.
Kaasalainen, M., Torppa, J., Muinonen, K., 2001. Optimization methods for asteroid lightcurve inversion. II. The complete inverse problem. Icarus 153, 37–51.
Keller, H.U. et al., 2007. OSIRIS: The scientific camera system onboard Rosetta. Space Sci. Rev. 128, 433–506.
Keller, H.U. et al., 2010. E-type Asteroid (2867) Steins as imaged by OSIRIS on Board Rosetta. Science 327 (5962), 190–193.
Kunszt, P.Z., Szalay, A.S., Thakar, A.R., 2001. The Hierarchical Triangular Mesh, Mining the Sky: Proceedings of the MPA/ESO/MPE Workshop Held at Garching, Germany, July 31 - August 4, p. 631.
Lamy, P.L. et al., 2008a. Asteroid 2867 Steins. III. Spitzer Space Telescope observations, size determination, and thermal properties. Astron. Astrophys. 487, 1187–1193.
Lamy, P.L. et al., 2008b. Asteroid 2867 Steins. II. Multi-telescope visible observations, shape reconstruction, and rotational state. Astron. Astrophys. 487, 1179–1185.

Lamy, P.L., Faury, G., Jorda, L., Kaasalainen, M., Hviid, S.F., 2010. Multi-color, rotationally resolved photometry of asteroid 21 Lutetia from OSIRIS/Rosetta observations. Astron. Astrophys. 521, A19.
Macke, R.J., Britt, D.T., Consolmagno, G.J., 2009. Enstatite chondrite physical properties: Density, porosity and magnetic susceptibility. Lunar Planet. Sci. 40, 1598 (abstracts).
McEwen, A.S., 1996. A precise lunar photometric function. Lunar Planet. Sci. 27, 841 (abstracts).
Oberst, J., Mottola, S., di Martino, M., Hicks, M., Buratti, B., Soderblom, L., Thomas, N., 2001. A model for rotation and shape of Asteroid 9969 Braille from ground-based observations and images obtained during the Deep Space 1 (DS1) flyby. Icarus 153, 16–23.
Ostro, S.J. et al., 2006. Radar imaging of binary near-Earth Asteroid (66391) 1999 KW4. Science 314, 1276–1280.
Richardson, J.E., Melosh, H.J., Greenberg, R.J., O'Brien, D.P., 2005. The global effects of impact-induced seismic activity on fractured asteroid surface morphology. Icarus 179, 325–349.
Rosten, E., Porter, R., Drummond, T., 2010. FASTER and better: A machine learning approach to corner detection. IEEE Trans. Pattern Anal. Mach. Intelligence 32, 105–119.
Rubincam, D.P., 2000. Radiative spin-up and spin-down of small asteroids. Icarus 148, 2–11.
Spjuth, S., Jorda, L., Lamy, P.L., Keller, H.U., Li, J.-Y., 2012. Disk-resolved photometry of Asteroid (2867) Steins. Icarus, submitted for publication.
Stooke, P.J., Abergel, A., 1991. Morphology of the nucleus of Comet P/Halley. Astron. Astrophys. 248, 656–668.
Thomas, P.C. et al., 1999. Mathilde: Size, shape, and geology. Icarus 140, 17–27.
Thomas, P.C. et al., 2002. Eros: Shape, topography, and slope processes. Icarus 155, 18–37.
Thomas, P.C. et al., 2007. The shape, topography, and geology of Tempel 1 from Deep Impact observations. Icarus 187, 4–15.
Thomas, P.C., Veverka, J., Simonelli, D., Helfenstein, P., Carcich, B., Belton, M.J.S., Davies, M.E., Chapman, C., 1994. The shape of Gaspra. Icarus 107, 23–36.
Thomas, P.C., Belton, M.J.S., Carcich, B., Chapman, C.R., Davies, M.E., Sullivan, R., Veverka, J., 1996. The shape of Ida. Icarus 120, 20–32.
Weissman, P.R., Hicks, M.D., Abell, P.A., Choi, Y.-J., Lowry, S.C., 2008. Rosetta target Asteroid 2867 Steins: An unusual E-type asteroid. Meteorit. Planet. Sci. 43, 905–914.
Werner, R.A., Scheeres, D.J., 1996. Exterior gravitation of a polyhedron derived and compared with harmonic and mascon gravitation representations of Asteroid 4769 Castalia. Celest. Mech. Dynam. Astron. 65, 313–344.